PHYSICAL REVIEW A **108**, 052805 (2023)

Role of the different electron capture processes in the molecular fragmentation dynamics in an Ar^{8+}-N_2 collision system

Md Abul Kalam Azad Siddiki, Kamal Kumar, Jibak Mukherjee, Lokesh C. Tribedi, and Deepankar Misra[*]
Department of Nuclear and Atomic Physics, Tata Institute of Fundamental Research, Homi Bhabha Road, Colaba, Mumbai 400005, India

(Received 9 December 2022; accepted 16 October 2023; published 7 November 2023)

We study the electron capture-induced fragmentation of N_2 molecules upon impact with Ar^{8+} projectiles at collision velocities 0.4 and 1.0 a.u. The recoil ions and the charge-changing projectiles are recorded in coincidence by combining a cold target recoil ion momentum spectrometer with a projectile final charge state analyzer. The relative contributions between projectile autoionizations and radiative decays are measured for the individual dissociation pairs. The reaction windows and corresponding final projectile states for multiple-electron capture processes are estimated using the extended classical over-the-barrier model. The various dissociation pairs' kinetic energy release (KER) is measured for the associated capture processes. For the dissociating N_2^{m+} $(2 \leqslant m \leqslant 6)$ molecular ions, the mean KER values shifted to higher values as capture stabilization increased. The populations of the higher KER regions are explained by the recapture of the loosely bound electrons into the target highly excited states. A simple classical capture model is employed to understand the role of the different projectile states on the KER distributions (KERDs). Our findings thus demonstrate the collision velocity dependence of the projectile's final state populations and its impact on the KERDs in the highly perturbative regime.

DOI: 10.1103/PhysRevA.108.052805

I. INTRODUCTION

Charge-changing collisions of charged particles with neutral atoms and molecules have drawn much attention. In collision with slow ($\upsilon_p < 1.0$ a.u., where υ_p is the projectile or collision velocity) highly charged ions (HCIs), multiple electrons are captured into the projectile excited states. The study of relaxation pathways of these excited states and their influence on the collision dynamics is the subject of fundamental many-body dynamics [1–5]. Studies of its application are also extended to tokamak plasma and astrophysical environments [6,7]. In the multiple-electron capture (MC) process, the loosely bound outer electrons can also be recaptured by the target in the excited states. This is also known as the target transfer excitations (TE) process and electron-electron (*e*-*e*) correlation process [3,8,9]. For the MC process, the reaction window is predicted by the extended classical over-the-barrier (ECOB) model [10]. Several studies show that the ECOB model successfully predicts the reaction window for collision systems of HCIs with atoms and molecules [4,11–13].

When a few electrons are ejected from the target molecules, the resultant transient molecular ions could decay due to mutual Coulomb repulsion between the charged centers. The kinetic energy of the fragment ions from molecular fragmentation carries information corresponding to electronic states. With the advent of multiparticle coincidence three-dimensional momentum imaging techniques such as cold target recoil ion momentum spectroscopy (COLTRIMS) [14,15], kinematically complete experiments can be carried out. Good quality data could be obtained by employing both time and space focusing [16] to compensate for the finite interaction volume between the ion beam and the target. Numerous studies [12,17–21] have reported on ion-molecule collisions that were used to understand the fragmentation mechanisms for a wide range of interaction strength $S = q/\upsilon_p b$, where q is the projectile charge and b is the impact parameter between the collision partners. The introduction of fragmentation studies of complex molecules and van der Waals clusters has also opened up new dimensions [22]. This also reveals how electron rearrangements happen in the cases of covalent molecules and van der Waals clusters [23]. It has also been possible to realize some new kinds of relaxation channels [24,25]. Recently, Mery *et al.* [26] probed the effects of a molecular environment on molecular fragmentation dynamics.

To investigate the decay dynamics of multiply charged molecules in collision with high-charge and low-charge projectiles, N_2 is a prototype system. The molecular orbital configuration of the N_2 molecules is $1\sigma_g^2 1\sigma_u^2 2\sigma_g^2 2\sigma_u^2 1\pi_u^4 3\sigma_g^2$. The outer valence orbitals $(2\sigma_u^2 1\pi_u^4 3\sigma_g^2)$ contain eight electrons with binding energies between 14.2 and 18.1 eV, and the $2\sigma_g^2$ orbital defines the inner valence orbital electrons [27]. Seigmann *et al.* [28] studied the Coulomb explosion of N_2 molecules induced by fast, highly charged projectiles (5.9 MeV/u Xe^{18+} and Xe^{43+}) and showed the kinetic energy release (KER) dependence on the perturbation strength ($\kappa = q/\upsilon_p$). In this high-velocity range, the electron-capture cross section is very small, and target ionization is the dominant process [29]. Mizuno *et al.* [30] showed the dependence of the KER of the N_2^{2+} dissociation for different charge-changing processes, including electron capture and loss by 2 MeV C^+

---

[*] Corresponding author: dmisra@tifr.res.in

projectiles. They found projectile electron loss, governed by the small impact parameters, dominantly populates the higher excited states. Renshelded *et al.* [31] studied the electron transfer for the Ar^{8+}-N_2 collision system at low energies (8–16 keV). Although the final projectile charges were detected coincidentally with recoil ions, the various projectile relaxation channels were not separated. They found that the dissociation mostly occurs from the lowest molecular states of the multicharged parent ion. Rajput *et al.* [32] studied the decay channels resulting from the 1.0 a.u. Ar^{9+}-N_2 collision system. The transfer ionization (TI) process also contributes in this velocity range [33,34]. The experiment did not detect the projectile ions, and the KER distributions (KERDs) consist of TI, projectile autoionization, and pure ionization processes. Therefore, further studies are needed to understand the possible capture-associated mechanisms. The dependence of molecular fragmentation on the various capture paths will shed light on the involved collision dynamics. In ion-atom and ion-molecule collisions, the amount of energy deposited to the target is governed by the impact parameters between the collision partners [18]. This results in different populations of the excited electronic states of the transient molecular ions. The branching ratios among the different decay channels carry rich information about the ongoing capture-associated processes. Measurement of the fragmentation yields for different capture-associated channels will reflect the possible impact parameter ranges of the underlying charge exchange collision dynamics.

In this paper, we have studied the role of the various capture-associated processes in the fragmentation (dissociation) dynamics by slow ($\upsilon_p = 0.4$ a.u.) and intermediate ($\upsilon_p = 1.0$ a.u.) velocity Ar^{8+}-N_2 collisions. The impact of the capture-associated processes on the KERDs was analyzed for the various dissociation channels. The reaction windows for the different dissociation channels are calculated using the ECOB model. In the intermediate collision velocity, electron-capture processes are accompanied by the TI processes. The relative contributions of the various capture pathways are also analyzed.

The paper is organized as follows: A brief description of the experimental methods is given in Sec. II, the data analysis is explained in Sec. III, the ongoing collision processes are introduced in Sec. IV, results and discussion of the various dissociation channels are presented in Sec. V, and the conclusions are given in Sec. VI.

II. EXPERIMENTAL DETAILS

The experiments were performed in the electron cyclotron resonance-based ion accelerator (ECRIA) [35] facility at the Tata Institute of Fundamental Research (TIFR) using the COLTRIMS imaging system [36]. The Ar^{8+} projectile beams with collision velocities 0.4 and 1.0 a.u. interact perpendicularly with the supersonically cold N_2 jet. The cold jet is produced by expanding N_2 gas through 30 μm aperture with a stagnation pressure of 2 bar. A double-stage skimmer assembly further skims the jet. After the interaction, the charge-changing projectiles following electron capture with the targets are analyzed using a trapezoidal electrostatic charge state analyzer (CSA). The main projectile beam is vertically deflected towards a Faraday cup mounted in the assembly of the projectile detector. The projectile detector detects the other charge-changing projectile ions downstream around 1.2 m from the interaction region. The recoil ions are guided by the vertical electric fields and detected by the recoil detector. For both recoil and projectile detectors, we used the 80 mm diameter microchannel plate (MCP) followed by the delay line anode (DLA) detector (MCP + DLA) [37]. The projectile hits give the start signal and opens a time window of a few μs to detect the recoil ions. The time window is adjustable in the program. For the Ar^{8+}-N_2 collision system, we put a 10 μs window sufficient for collecting all the recoil ions. The data are stored in an event-by-event list mode using the COBOLD PC software for offline analysis. The electric fields in the extraction and acceleration regions are 173.33 and 250.67 V/cm, respectively, which ensures a 13 eV 4π sr collection for singly charged recoil ions. An electrostatic beam cleaner was used to avoid primary projectile beam contamination due to the electron capture with residual gases throughout the beam line. Electrostatic deflector pairs were also used to appropriately interact the projectile beams with localized targets by compensating for the projectile beam deflections due to the spectrometer fields. Details can be found elsewhere [36,38]. Typically the beam current was maintained around 200 pA. Fig. 1 presents the schematic picture of the complete experimental setup.

III. DATA ANALYSIS

In order to calculate the kinetic energy of the recoil ions, the three-dimensional momentum vectors need to be constructed. The momentum components are calculated by using the equations

$$p_x = \frac{m(X - X_0)}{fT}, \tag{1}$$

$$p_y = \frac{m(Y - Y_0)}{fT} - p_{\text{jet}}, \tag{2}$$

and

$$p_z = -Cq_r E_s \Delta T. \tag{3}$$

m and q_r are the mass and charge of the recoil ion, respectively. X and Y denote the detector hit positions. The X_0 and Y_0 quantities are calculated using momentum conservation between the fragmented recoil ions pair. p_{jet} represents the momentum due to the jet velocity along the jet propagation direction. The quantity T is the time of flight (TOF), and E_s is the source electric field. $\Delta T = T - T_0$ represents the TOF difference between the nonzero p_z momentum component and the zero p_z component. The quantities C and f are the correction factors due to the lens. The corresponding kinetic energy (KE) for the ith ion with mass m_i is

$$\text{KE}_i = \frac{p_{ix}^2 + p_{iy}^2 + p_{iz}^2}{2m_i}. \tag{4}$$

KER is the sum of the KE of all recoil ions resulting from the dissociating parent molecular ions. Here, for the diatomic molecular case, KER is written as

$$\text{KER} = \text{KE}_1 + \text{KE}_2. \tag{5}$$

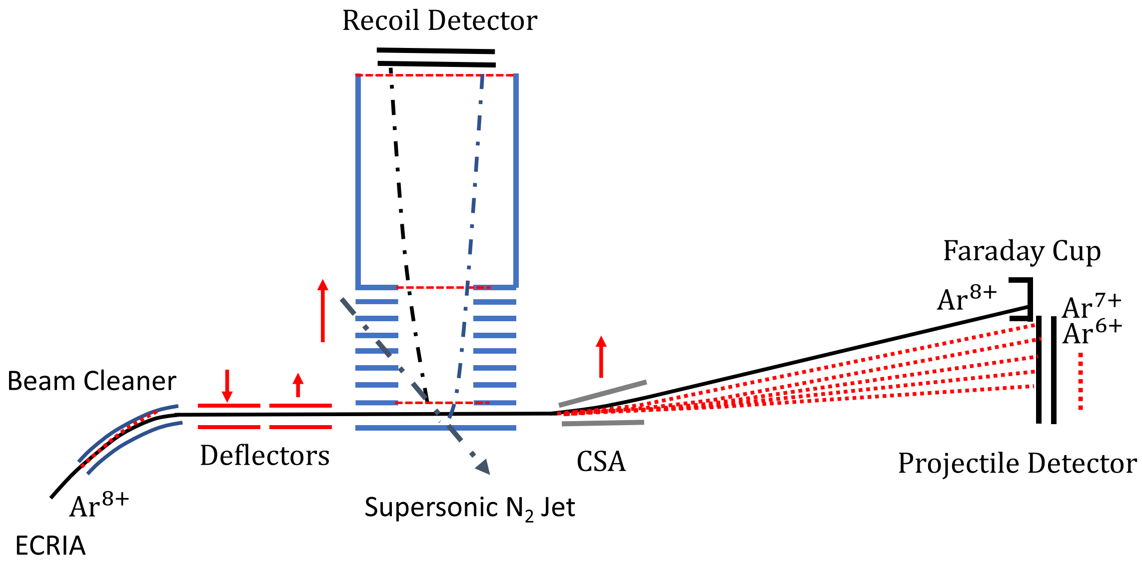

FIG. 1. Schematic diagram of the experimental setup. After the interaction, the fragment recoil pairs (dash-dotted lines) are guided towards the recoil detector, and the main projectile beam (Ar^{8+}, solid line) is deflected towards the Faraday cup while the other charge-changing projectiles (Ar^{7+}, Ar^{6+}, etc., dotted lines) hit the projectile detector. The solid red arrows define the respective electric field's direction. The length of the solid red arrows is proportional to the strength of the corresponding electric field for $\upsilon_p = 0.4$ a.u. Ar^{8+}-N_2 collisions.

A detailed analysis of the measurement of KER for a coincidence pair is discussed elsewhere [16].

IV. COLLISION PROCESSES

According to Bohr-Lindhardt's classical over-the-barrier (COB) model [39], electron capture is a two-step process. First, the electron is released from the target at a distance (R_r) when the projectile Coulomb attraction force (q/R_r^2) equals the binding force (υ_e^2/a) of the electron in the target. The corresponding release radius can be written as

$$R_r = \frac{(qa)^{1/2}}{\upsilon_e}, \tag{6}$$

where υ_e and a are the electron orbital velocity and radius, respectively. Second, the electron capture will occur when the electron kinetic energy ($m_e\upsilon_p^2/2$) is balanced by the potential energy ($-q/R$), which binds the electron into the final projectile state. The respective capture radius (R_c) is

$$R_c = \frac{2q}{\upsilon_p^2}. \tag{7}$$

In slow collisions ($\upsilon_p < 1$), when $R_c < R_r$ the released electron will be captured. The capture cross section is given by $\sigma_c = \pi R_r^2$, which is independent of υ_p. During the collisions, a released but uncaptured electron will be emitted if the energy transferred from the projectile ion is larger than the ionization energy of the quasimolecular states. The ionization radius (R_I) staifies

$$\frac{q}{R_I} \geqslant I + \frac{q}{R_r}, \tag{8}$$

where I is the ionization energy. A detailed discussion of this classical over-the-barrier ionization model is given in Refs. [40,41]. The ionization process ($R_c < R_I < R_r$) is determined by the total release probability (R_r/υ_p) and its uncaptured fraction ($1 - \frac{2q}{R_r}\frac{1}{\upsilon_p^2}$). The competition between these gives rise to the maximum ionization probability. The Bohr-Lindhardt model shows that the capture cross section is independent of υ_p in our investigated collision velocity range. However, with increasing υ_p, the uncaptured fraction of release probability increases, and the ionization process will not be negligible. Though our experiment is not sensitive to pure ionization processes, pure capture and capture associated with ionization processes are recorded.

In this Ar^{8+}-N_2 collision system, for $\upsilon_p = 0.4$ a.u., electron capture is the dominant process. The transfer ionization (TI) process is less probable in these slow collision regimes. TI is defined as one or multiple target electrons being ionized along with one or multiple electrons being captured in the projectile. As collision velocity increases to 1.0 a.u., the TI process also becomes a contributing process along with capture. Detailed discussions on the interplay between the various collision processes for slow and intermediate collision velocities can be found in [32,42,43]. For simplicity of discussion, we have ignored the less probable TI process for the $\upsilon_p = 0.4$ a.u. Here, in a collision with a highly charged projectile like Ar^{8+}, multiple electrons are captured into the projectile excited states. Projectile single or multiple autoionizations could happen if these excited states stay above the ionization threshold. We have labeled the multiple captures ($m \geqslant 3$) followed by the one or multiple projectile autoionizations and radiative decays through the equation

$$\begin{aligned} \mathrm{Ar}^{q+} + \mathrm{N}_2 &\rightarrow \mathrm{Ar}^{(q-m)+**\cdots} + \mathrm{N}^{r+} + \mathrm{N}^{s+} \\ &\rightarrow \mathrm{Ar}^{(q-m+n)+} + ne^-_{\mathrm{An}} \\ &\quad + \sum_k h\nu_k + \mathrm{N}^{r+} + \mathrm{N}^{s+} \quad (\mathrm{C}m\mathrm{A}n), \end{aligned} \tag{9}$$

where $m = r + s$ and m is the number of captured electrons. Here, n is the number of the projectile autoionizing electrons, and k denotes the number of radiative photons. The quantity in parentheses defines the ongoing capture process. For example, the C3A1 channel indicates that triple-electron capture is followed by single projectile autoionization.

In the case of multiple electron capture not followed by the projectile autoionization, the projectile excited states stabilize through photon emissions. This process is known as radiative stabilization. Capture stabilization increases as the number of projectiles autoionizing electrons is reduced. For the most straightforward double-electron capture (DC) processes, radiative stabilization is referred to as a true double-electron capture (TDC). On the other hand, the DC is followed by projectile autoionization, named the autoionizing double-electron capture (ADC) process.

At $\upsilon_p = 1$ a.u., TI is also a contributing process. The simplest TI process is single-electron capture and ionizing another target electron (TI = SC + SI). Therefore, MC, followed by projectile autoionizations and radiative decays, contributes in addition to the ionization process. The processes could be written as

$$\begin{aligned}\mathrm{Ar}^{q+} + \mathrm{N}_2 &\rightarrow \mathrm{Ar}^{(q-m)+**\cdots} + je^-_{Ij} + \mathrm{N}^{r+} + \mathrm{N}^{s+}\\ &\rightarrow \mathrm{Ar}^{(q-m+n)+} + ne^-_{\mathrm{An}}\\ &\quad + \sum_k h\nu_k + je^-_{Ij} + \mathrm{N}^{r+} + \mathrm{N}^{s+} \quad (\mathrm{C}m\mathrm{A}n + I_j).\end{aligned} \tag{10}$$

Here, $m + j = r + s$, and j is the number of ionized electrons. The collision process is defined as $(\mathrm{C}m\mathrm{A}n + I_j)$. For $j = 1$ and 2, I_1 and I_2 are known as single ionization (SI) and double ionization (DI). For example, Triple-electron capture (TC) followed by single autoionization in addition to single ionization could be written as a $(\mathrm{C3A1} + I_1)$ or (C3A1 + SI).

V. RESULTS AND DISCUSSION

In collisions with Ar^{8+} projectile ions, multiple electrons are removed from the N_2 molecules. The parent transient N_2^{m+} molecular ions fragment into daughter $\mathrm{N}^{r+} + \mathrm{N}^{s+}$ ions if the corresponding states are repulsive in nature. The decay of multiple excited states results in different peaks in the KER distributions. Figure 2 shows the ion-ion coincidence spectrum for the $\upsilon_p = 0.4$ a.u. Ar^{8+}-N_2 collision system. The various symmetric ($r = s$), nearly symmetric, ($r = s + 1$), and asymmetric ($r = s + 2$) fragmentation channels are indicated in this figure. One can see that the collection efficiencies of the various channels are limited to their much higher KER and asymmetric charge sharing.

The KERDs for each dissociation channel were measured in coincidence with the final projectile charge states. This correlates to the variation in the KERDs with the impact parameters for various capture-associated processes. The projection of the projectile image along the beam deflection is plotted for each dissociation pair. Figure 3 shows the interplay between the different capture-associated processes with υ_p for the individual dissociation pairs. The relative yields of the various capture processes at $\upsilon_p = 0.4$ and 1.0 a.u. are tabulated in Tables I and II, respectively. The corresponding mean KER values and widths (FWHM) are also given. The 4π sr collections for the different fragmentation channels

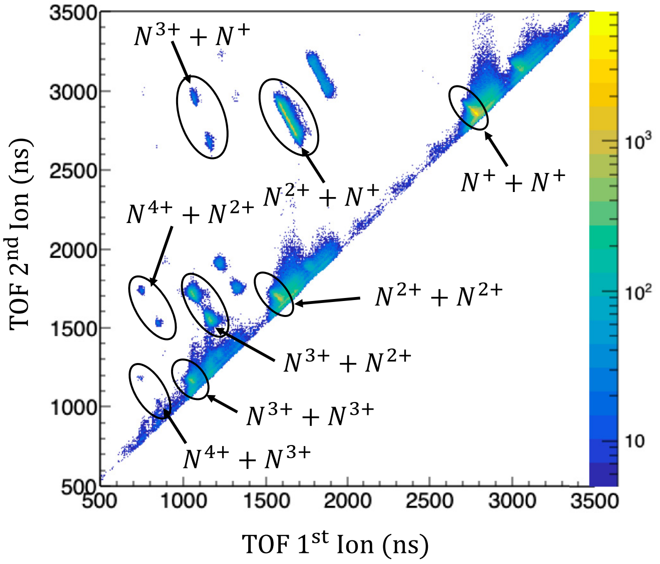

FIG. 2. Ion-ion coincidence spectrum for the Ar^{8+}-N_2 collision system at $\upsilon_p = 0.4$ a.u. The various $\mathrm{N}^{r+} + \mathrm{N}^{s+}$ dissociation pairs are measured in coincidence with final charge-changing projectiles. The color bar in the right side represents the counts of the different dissociation pairs.

$(\mathrm{N}^{r+} + \mathrm{N}^{s+})$ are not the same due to higher KER values and asymmetric charge sharing. Here, the total collection is almost independent of the capture path for a specific dissociation pair. However, the KERDs variation with associated capture paths could underestimate the yield for the higher KER values.

In the electron capture at the collision velocities investigated here, the collision time is around a few hundred attoseconds. This is quite fast compared to the nuclear motions in tens of femtoseconds. Hence, the ejection of target electrons will happen for frozen internuclear separations (R_e). Therefore, using the reflection principle [44], one may employ the Coulomb explosion model (CEM). It is an approximation of the pure Coulomb repulsive dissociation path to compare with the KER of the resulting fragmentation channels as below:

$$\mathrm{KER(eV)} = 14.4\frac{rs}{R_e(\text{Å})}, \tag{11}$$

where for the N_2 molecule $R_e \simeq 1.09$ Å.

The ECOB model is employed for the HCI-molecule collisions when the collision time is shorter than the molecule vibration time [9]. The various dissociation channels' reaction windows can be predicted for the MC process using the ECOB model [10]. Assuming a Gaussian distribution of a Q value around the calculated mean Q value $Q_0^{(j)}$, the Q-value distribution for a given capture string j can be written as

$$W(Q) = \frac{1}{\Delta Q^{(j)}\sqrt{\pi}} \exp\left[-\left(\frac{Q - Q_0^{(j)}}{\Delta Q^{(j)}}\right)^2\right]. \tag{12}$$

The quadratic sum of all captured electrons in the total energy uncertainty of the Q value for certain capture string j is given

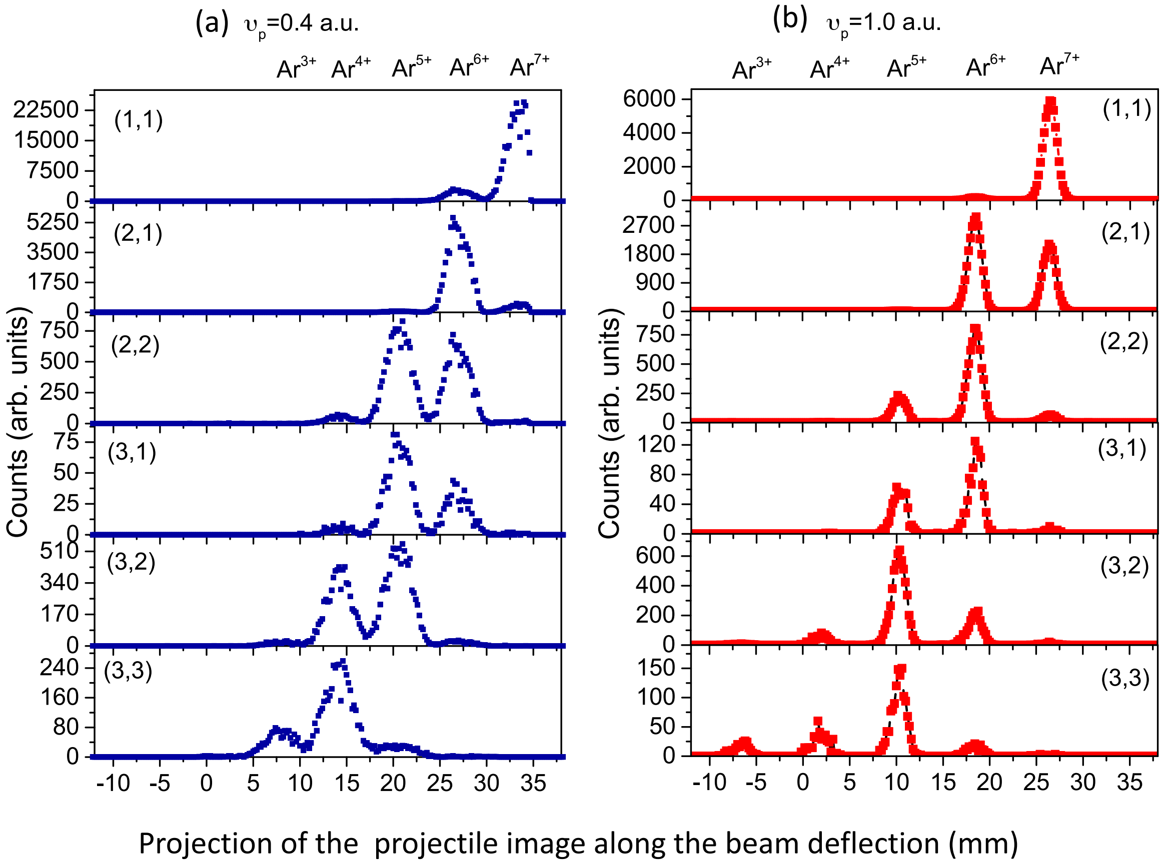

FIG. 3. The projections of the charge-changing projectile ions in the beam deflection for the various dissociation channels ($N^{r+} + N^{s+}$) of transient N_2^{m+} molecular ions at (a) $\upsilon_p = 0.4$ a.u. and (b) 1.0 a.u. Charge sharing (r, s) of the dissociating pairs is given in parentheses.

by

$$\Delta Q = \left[\sum_t \left(\Delta E_t^{(j)}\right)^2 \right]^{0.5}. \tag{13}$$

The mean Q value for a given string can be calculated using the formula

$$Q_0^{(j)} = \sum_t \left(\epsilon_t^{(j)} - I_t\right), \tag{14}$$

where $\sum_t \epsilon_t^{(j)}$ is the sum of binding energies of the captured electrons, and I_t is the ionization potentials. The mean of a reaction window for a given string is defined by $\sum_t \epsilon_t^{(j)}$. The binding energies of the t electron in the case of capture by a projectile or recapture by the target can be estimated using this ECOB model. Figure 4 shows the calculated reaction windows around the mean value $\sum_t \epsilon_t^{(j)}$. For simplicity, the distributions are normalized to unity [13].

TABLE I. Relative fragmentation yields (in %) of the different capture-associated channels for the $\upsilon_p = 0.4$ a.u. Ar^{8+}-N_2 collision system. The corresponding mean KER (eV) value and the KER width (FWHM, in parentheses) in eV are given below.

Dissociation channel			Final projectile		
	Ar^{7+}	Ar^{6+}	Ar^{5+}	Ar^{4+}	Ar^{3+}
$N^+ + N^+$	92.6 ± 0.3 7.6 (1.8)	7.4 ± 0.1 18.7 (9.2)			
$N^{2+} + N^+$	7.3 ± 0.1 18.7 (2.0)	91.2 ± 0.4 22.5 (2.0)	1.5 ± 0.1		
$N^{2+} + N^{2+}$	1.3 ± 0.1 42.5 (12.5)	49.9 ± 0.7 42.8 (15.3)	46.1 ± 0.7 53.0 (23.7)	2.7 ± 0.2 70.8 (39.9)	
$N^{3+} + N^+$	0.7 ± 0.2	28.7 ± 1.4 43.4 (15.4)	66.1 ± 2.1 52.2 (27.6)	4.5 ± 0.5	
$N^{3+} + N^{2+}$		2.4 ± 0.1 66.3 (24.2)	56.2 ± 0.6 71.7 (27.0)	39.1 ± 0.5 85.1 (31.7)	2.2 ± 0.1 102.1 (39.4)
$N^{3+} + N^{3+}$		1.0 ± 0.1	9.8 ± 0.4 96.1 (29.3)	69.1 ± 1.2 101.7 (26.2)	20.1 ± 0.6 114.4 (34.9)

TABLE II. Relative fragmentation yields (in %) of the different capture-associated channels for the $\upsilon_p = 1.0$ a.u. Ar^{8+}-N_2 collision system. The corresponding mean KER (eV) value and the KER width (FWHM, in parentheses) in eV are given below.

Dissociation channel	Final projectile Ar^{7+}	Ar^{6+}	Ar^{5+}	Ar^{4+}	Ar^{3+}
$N^{+} + N^{+}$	97.3 ± 0.4 7.6 (1.8)	2.7 ± 0.1 16.5 (9.7)			
$N^{2+} + N^{+}$	41.4 ± 0.3 18.7 (2.0)	58.2 ± 0.4 21.8 (2.0)	0.4 ± 0.1		
$N^{2+} + N^{2+}$	5.1 ± 0.2 43.1 (17.9)	66.7 ± 0.7 45.4 (18.9)	27.8 ± 0.5 56.3 (28.1)	0.4 ± 0.1	
$N^{3+} + N^{+}$	3.1 ± 0.4	61.1 ± 1.9 46.0 (17.2)	35.3 ± 1.5 52.7 (23.5)	0.5 ± 0.2	
$N^{3+} + N^{2+}$	1.1 ± 0.1	22.9 ± 0.5 72.9 (28.1)	67.6 ± 0.9 77.6 (31.6)	7.6 ± 0.3 84.9 (32.3)	0.8 ± 0.1
$N^{3+} + N^{3+}$	0.8 ± 0.2	8.5 ± 0.6 102.1 (30.4)	59.6 ± 1.6 103.9 (31.2)	20.8 ± 1.0 108.7 (32.2)	10.3 ± 0.7 114.8 (33.5)

The width of the reaction window shows a variation with $\upsilon_p^{0.5}$ [10]. As collision velocity increases, the reaction window broadens, and more projectile states are accessible. The populations of the higher *nl* projectile states (*n* and *l* are the principal and the orbital quantum numbers, respectively) also increase. This can be understood as the captured electron moving with the projectile and is subjected to a higher angular momentum in the projectile frame as follows:

$$\vec{L} = \vec{R}_c \times m_e \vec{\upsilon}_p, \tag{15}$$

where R_c is the capture radius that defines the impact parameter. For single-electron capture, R_c is around 11.9 a.u., calculated from the ECOB model. At $\upsilon_p = 1.0$ a.u., $|\vec{L}|$ is around 11.9 a.u. It is large enough to account for the population enhancement towards the states with a large angular momentum projection on the axis perpendicular to the collision plane. Also, with increasing υ_p, the mean Q value decreases, indicating the stronger populations towards the higher *nl* states [45].

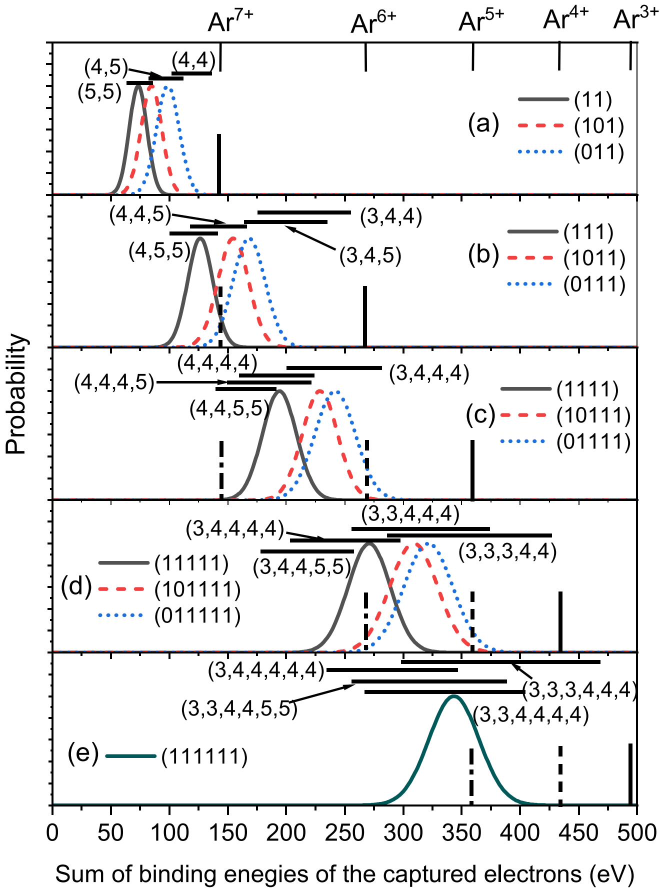

FIG. 4. Reaction windows for different capture strings are calculated using the ECOB model for the $\upsilon_p = 0.4$ a.u. Ar^{8+}-N_2 collision system. The horizontal black solid lines indicate the energy range, and the respective principal quantum numbers of the final projectile states are given in parentheses. Thresholds for the single, double, and triple autoionization are marked by the solid, dashed, and dash-dotted vertical lines (right to left).

According to the ECOB model, the multiple electrons are assigned to a string where 1 represents the electron captured by the projectile, and 0 represents the electron recaptured by the target. For example, for the three-electron process, the (011) string indicates that the projectile captures the second and the third electrons while the target recaptures the first electron into the excited states. Here, in the ECOB calculation, the first, second, and third electron ionization energies correspond to the ionization energies of the ground electronic states of N_2, N_2^+, and N_2^{2+}, respectively. The position of the string from left to right corresponds to the sequence in which electrons become molecular in the quasitriatomic $(ArN_2)^{8+}$ molecular ion during the collision. In the frozen-core approximation, the ionization energies for the ground electronic states of the multiply charged N_2^{m+} ($m \leqslant 6$) molecular ions [31,32,46] are calculated by the coupled clusters single and doubles (CCSD) method using the cc-pVDZ basis set [47]. The binding energies of the final projectile states for various *nl* configurations are calculated by the flexible atomic code (FAC) [48].

In the following subsections, we discuss the dissociation of the multiply charged transient N_2^{m+} molecular ions ($2 \leqslant m \leqslant 6$) for the various capture-associated mechanisms.

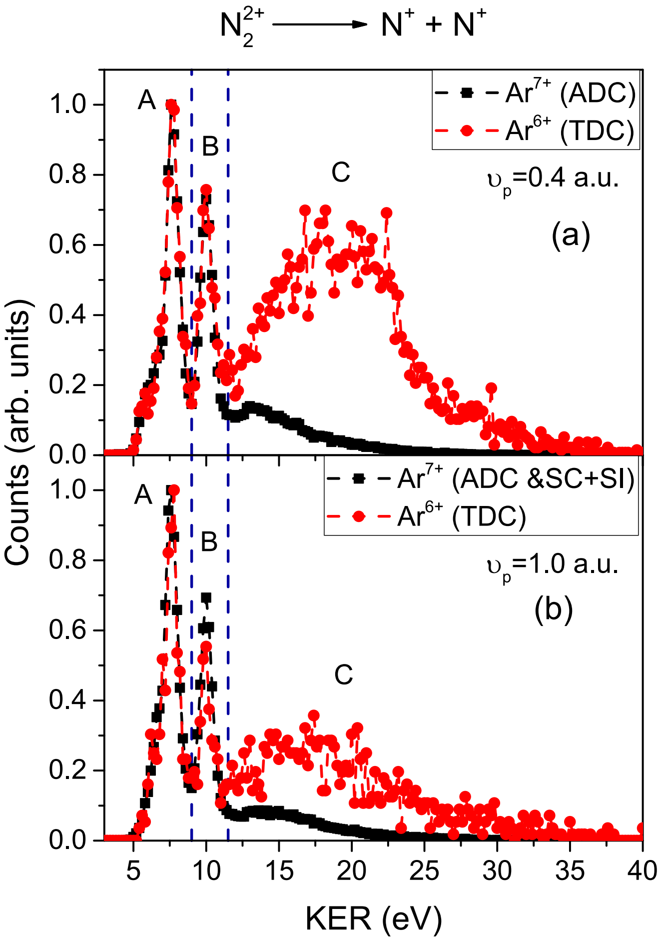

FIG. 5. Normalized KER spectra of the $N^+ + N^+$ dissociation channel for different capture associated processes at (a) $\upsilon_p = 0.4$ a.u. and (b) 1.0 a.u.

A. Dissociation of N_2^{2+}

The parent N_2^{2+} ions break up into $N^+ + N^+$ pairs. The KERDs for both collision velocities are presented in Fig. 5. The various electronic states for the corresponding KER are tabulated in Table III. For simplicity, we have separated the KERDs into three different regions, as indicated in Fig. 5. These are A ($5 \leqslant \text{KER} \leqslant 9$ eV), B ($9 \leqslant \text{KER} \leqslant 11.5$), and C ($\text{KER} \geqslant 11.5$).

For $\upsilon_p = 0.4$ a.u., TDC and ADC are the two possible capture paths. The ADC channel has $92.6 \pm 0.3\%$, resulting in it being the dominant process, whereas TDC only contributes around $7.4 \pm 0.1\%$. At $\upsilon_p = 1.0$ a.u., the populations towards higher nl ($n \geqslant 5$) states increase as electrons in the projectile frame see higher angular momentum. These states have higher autoionization yields. This results in a lower relative yield of the TDC process, around $2.7 \pm 0.1\%$. Also, with increasing υ_p, the contribution of the TI (SC + SI) is not negligible and mixes with the ADC channel [49].

TABLE III. Various electronic states and corresponding KERs of the N^+-N^+ fragmentation channels.

Electronic states	KER (eV)	Dissociation limit
$A^1\Pi_u[3\sigma_g^{-1}1\pi_u^{-1}]$	6.8 ± 0.2	$N^+(^3P) + N^+(^3P)$
$D^3\Pi_g[2\sigma_u^{-1}1\pi_u^{-1}]$, $C^1\Sigma_g^+[1\pi_u^{-2}]$, and $B^1\Delta_g[1\pi_u^{-2}]$	7.4 ± 0.2	$N^+(^3P) + N^+(^3P)$
$D^1\Sigma_u^+[2\sigma_u^{-1}3\sigma_g^{-1}]$, $1^1\Pi_g[2\sigma_u^{-1}1\pi_u^{-1}]$	10.0 ± 0.2	$N^+(^3P) + N^+(^1D)$
$1^1\Sigma_g^+[2\sigma_g^{-1}3\sigma_g^{-1}]$, $1^1\Sigma_u^+[2\sigma_g^{-1}2\sigma_u^{-1}]$		
Closely spaced repulsive high-lying states	Above 11.5	

TABLE IV. Relative fragmentation yields (in %) of the different KER regions of the $N^+ + N^+$ dissociation channel for $\upsilon_p = 0.4$ and 1.0 a.u. Ar-N_2 collision systems.

Capture channel	υ_p (a.u.)	Region A	Region B	Region C	Final projectile
ADC	0.4	44.9 ± 0.2	29.3 ± 0.2	25.7 ± 0.2	Ar^{7+}
TDC	0.4	15.5 ± 0.5	11.3 ± 0.4	73.1 ± 1.1	Ar^{6+}
ADC+TI	1.0	49.9 ± 0.3	28.6 ± 0.2	21.5 ± 0.2	Ar^{7+}
TDC	1.0	25.5 ± 1.3	12.8 ± 0.9	61.6 ± 2.0	Ar^{6+}

At both collision velocities, the KERDs show a noticeable population variation for the various capture channels (ADC, TDC, TI). For the TDC process, the higher KER region (C) has the dominant population of around ~73%. On the other hand, for ADC and TI processes, the lower KER regions (A and B) have the dominant contributions of around ~74%. Depending upon the collision processes, the populations almost switch for low and high KER regions. The relative populations for each channel are tabulated in Table IV. The yield of the C region is slightly underestimated as the KER is extended past 26 eV, beyond the 4π sr collection for this dissociation channel.

We focus on the primary electron capture processes to understand the population variations in the ADC and TDC processes. The (11) string [cf. Fig. 4(a), solid line] defines the projectiles that capture the first and second electrons, mostly the loosely bound valence electrons. This leads to the populations of the electronic states around the ground state of the N_2^{2+} with a reaction window FWHM of ~10.8 eV. The dissociation of these states gives low-energy KER. The A region mostly arises from the (11) electron capture process. For the (101) string [cf. Fig. 4(a), dashed line], the projectile captures the first and third electrons while the target recaptures the second electron into the excited states of N_2^{2+*}. According to the ECOB calculations, the binding energy of the recaptured electron is around ~31.4 eV with respect to the ground electronic state of the N_2^{3+} molecular ions. The potential energy of the N_2^{3+} ($^2\Pi_u$) ground electronic state is calculated around 84 eV with respect to the ground electronic state of the neutral N_2 ($^1\Sigma_g^+$) molecules. The corresponding electronic states vertically along the Franck-Condon (FC) region of N_2^{2+*} stay around $(84–31.4) = 52.6$ eV with a FWHM of ~8.7 eV. In the case of the (011) string [cf. Fig. 4(a), dotted line], the projectile captures the second and third electrons while the target recaptures the first electron. The binding energy of the first electron is ~22 eV. It results in a population of high-lying electronic states of N_2^{2+*} around $(84–22) = 62$ eV with a FWHM ~6.7 eV. It can be seen that the dissociation of these states resulting from (101) and (011) capture processes

TABLE V. Relative fragmentation yields (in %) of the different KER regions of the $N^{2+} + N^{+}$ dissociation channel for $\upsilon_p = 0.4$ and 1.0 a.u. Ar-N_2 collision systems.

Capture channel	υ_p (a.u.)	Lower KER $(D+E+F+G)$	Higher KER (H)	Final projectile
C3A2	0.4	87.7 ± 1.2	12.3 ± 0.5	Ar^{7+}
C3A1	0.4	80.7 ± 0.3	19.3 ± 0.2	Ar^{6+}
C3A2+(ADC+SI)	1.0	81.8 ± 0.7	18.2 ± 0.3	Ar^{7+}
C3A1+(TDC+SI)	1.0	70.9 ± 0.5	29.1 ± 0.3	Ar^{6+}

could lead to lower (B) and higher (C) KERDs where the mean KER values are separated by ~10 eV. The density of the electronic states in these higher excited states is very large, so assigning the exact excited state is difficult. The broad KERDs around 20 eV also imply a broad range of many excited states decaying to the different dissociation limits.

The calculated reaction window [cf. Fig. 4(a)] shows that the A region mostly comes from the excited (5,5) states of the Ar^{6+} ion. The B region mostly arises from overlapping the (5,5) and (4,5) configurations. The higher KER regions mostly come from the (4,5) and (4,4) configurations. All these configurations stay in the autoionization region. This leads to much higher ADC yields than the radiative stabilized TDC process. It was seen that the primarily populated $(4l, 4l')$ state for small internuclear separation is subsequently transferred to the asymmetric $(3l, nl)$ $(n > 9)$ Rydberg series at larger internuclear separations. This process is known as an autotransfer to Rydberg states (ATR) and enhances the fluorescence yield [50]. It was also seen that the population of the C region for the TDC process decreases from $73.1 \pm 1.1\%$ to $61.6 \pm 2.0\%$ as υ_p increases from 0.4 to 1.0 a.u. In this C region, the TDC results through the ATR process of the (4,4) states mixing with the $(3l, nl)$ $(n > 9)$ Rydberg series. ATR is a postcollision effect that decreases with increasing collision velocity [51,52]. Therefore, as υ_p increases from 0.4 to 1.0 a.u., the relative yield of the C region decreases.

B. Dissociation of N_2^{3+}

In collision with the Ar^{8+} projectile ion, the resultant N_2^{3+} ion dissociates in to a pair of N^{2+} and N^{+} ions. The KERDs (cf. Fig. 6) for both collision velocities show distinct peaks at around 15.7 ± 0.3 (D), 18 ± 0.3 (E), 20.8 ± 0.3 (F), and 22.7 ± 0.3 (G) eV, and a broad continuum around 29 ± 2.0 (H) eV. The D, E, and G peaks represent the corresponding electronic states $^2\Pi$, $^4\Sigma$, and $^2\Sigma$ [21,32,53]. The broad peak H mostly comes from the closely spaced high-lying electronic states. The relative yields for the dominant capture-associated paths are tabulated in Table V.

For $\upsilon_p = 0.4$ a.u., the capture channels are pure triple-electron capture (C3A0), triple-electron capture followed by single autoionization (C3A1), and triple-electron capture followed by double autoionization (C3A2). The relative yields between the C3A2, C3A1, and C3A0 are 7.3%, 91.2%, and 1.5%, respectively.

The higher yield of the C3A1 channel explains the projectile final state populations being in (3,4,5), (3,4,4), and some of the lower angular orbital numbers of (4,4,5) states. The binding energies of these above states also stay in the single-autoionization regions. The threshold of the double autoionization is 216.5 eV (DI energy of Ar^{5+}) [54]. The (4,5,5) and the higher orbitals of the (4,4,5) configurations stay in the double-autoionization region. These states mostly lead to the C3A2 relaxation pathways. The reaction windows for the (111), (1011), and (0111) strings [cf. Fig. 4(b)] do not belong to the states below the first-autoionization limit. This results in the negligible contributions of the C3A0 process. It also shows the minor radiative stabilization ratio (around ~1.5%) for the N^{2+}-N^{+} dissociation process.

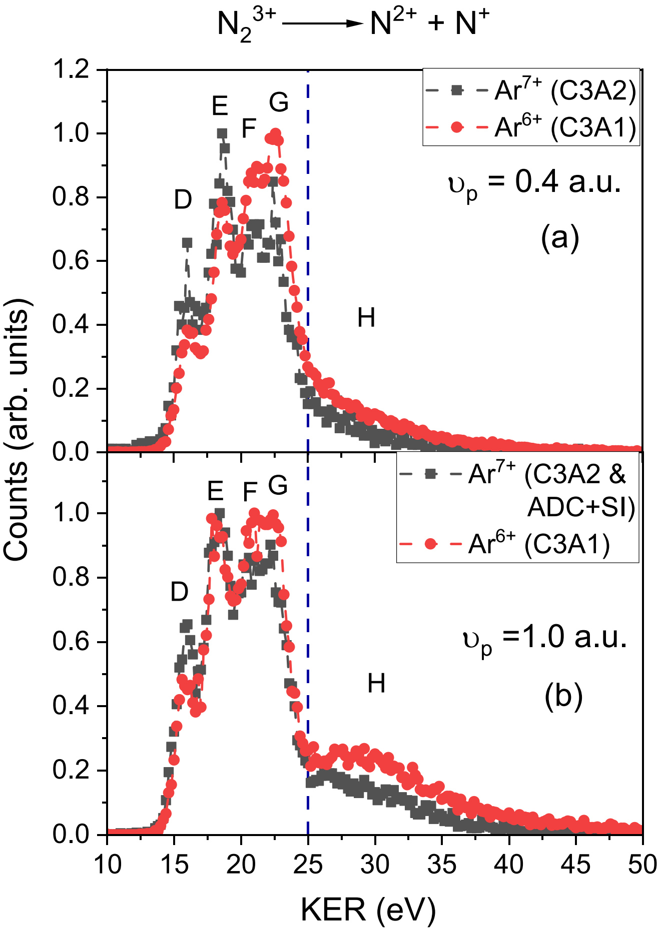

FIG. 6. Normalized KER spectra of the $N^{2+} + N^{+}$ dissociation channel for different capture associated processes at (a) $\upsilon_p = 0.4$ a.u. and (b) 1.0 a.u.

As capture stabilization increases from C3A2 to C3A0, the most probable KER value shifts toward a higher one, like E to G, for C3A2 to C3A1. Therefore, the above projectile states involved in the capture processes have different Q values, increasing with capture stabilization.

For $\upsilon_p = 1.0$ a.u., the partial yield of the capture channel associated with Ar^{7+} is enhanced from ~7.3% to 41.4%. The possible capture paths are C3A2, ADC in addition to single ionization (ADC + SI), and single-electron capture in addition to double ionization (SC + DI). However, at this υ_p, DI is a less probable event [55,56]. The reaction window is broadened, and populations to the higher nl states also increase as collision velocity increases from 0.4 to 1.0 a.u. Therefore, the electron capture process into the (4,4,5), (4,5,5), or some higher states increases, and stays in the double-autoionization region. These states could contribute significantly to the C3A2 process.

The ADC + SI channel also indicates that the projectile first captures two electrons, making the final state populations the autoionizing (4,5) and (5,5) states. For the capture path associated with Ar^{6+}, the possibility of TDC in addition to SI (TDC + SI) is significantly less as the yield of TDC is very small, as seen for the two-electron capture process. Therefore, it mostly results from the C3A2 and ADC + SI processes. The presence of the TI process in addition to electron-capture processes results in a higher yield for the higher KER region for the N^{2+}-N^{+} dissociation path.

C. Dissociation of N_2^{4+}

The transient parent N_2^{4+} molecular ions decay via $\mathrm{N}^{2+} + \mathrm{N}^{2+}$ (symmetric channel) and $\mathrm{N}^{3+} + \mathrm{N}^{+}$ (asymmetric channel).

The yield of symmetric channels is much higher than that of the asymmetric channel, which suggests equal charge sharing after rearrangements. However, due to asymmetric charge sharing for the $\mathrm{N}^{3+} + \mathrm{N}^{+}$ channel, the lesser 4π sr collection also slightly underestimates the yield.

For the symmetric channels, the KER values of different electronic states are explained in Refs. [28,31,32,53]. The relevant decay channels are given by

$$N_2^{4+}(^3\Sigma) \rightarrow N^{2+}(^2P) + N^{2+}(^2P), \quad \mathrm{KER} = 42.50\mathrm{eV} \quad (16)$$

and

$$N_2^{4+}(a^5\Sigma) \rightarrow N^{2+}(^2P) + N^{2+}(^4P), \quad \mathrm{KER} = 35.5\mathrm{eV} \quad (17)$$

and

$$N_2^{4+}(b^5\Sigma) \rightarrow N^{2+}(^2P) + N^{2+}(^4P), \quad \mathrm{KER} = 45.40\mathrm{eV}. \quad (18)$$

We found the KER values centered around 35.2 ± 0.4, 42.8 ± 0.4, and 53.0 ± 0.4 eV (cf. Fig. 7).

For $\upsilon_p = 0.4$ a.u., the most probable capture paths are quadruple-electron capture followed by single autoionization (C4A1) and quadruple-electron capture followed by double-autoionization (C4A2). Here C4A1 and C4A2 have contributions around 46.1 ± 0.7% and 49.9 ± 0.7%, respectively. As capture stabilization increases, the mean of the KER values shifts towards the higher KER values. For the C4A2 to C4A1 process, the mean KER value shifted from 42.8 ± 0.4 to 53.0 ± 0.4 eV, and the corresponding KER width (FWHM) was enhanced from 15.3 to 23.7 eV. This indicates the different ranges of final projectile state populations with different ranges of Q values during the capture process. The reaction windows shift towards lower projectile states when more bound electrons are captured. This results in a higher Q value, and the reaction window's corresponding width (FWHM) also increases [cf. Fig. 4(c)]. Therefore, during collisions, a wide range of electronic states are populated. The dissociation of many electronic states with different dissociation limits results in a large KER width. The larger KER width (FWHM) indicates the population of the wide ranges of repulsive electronic states, which increases as the capture stabilization increases.

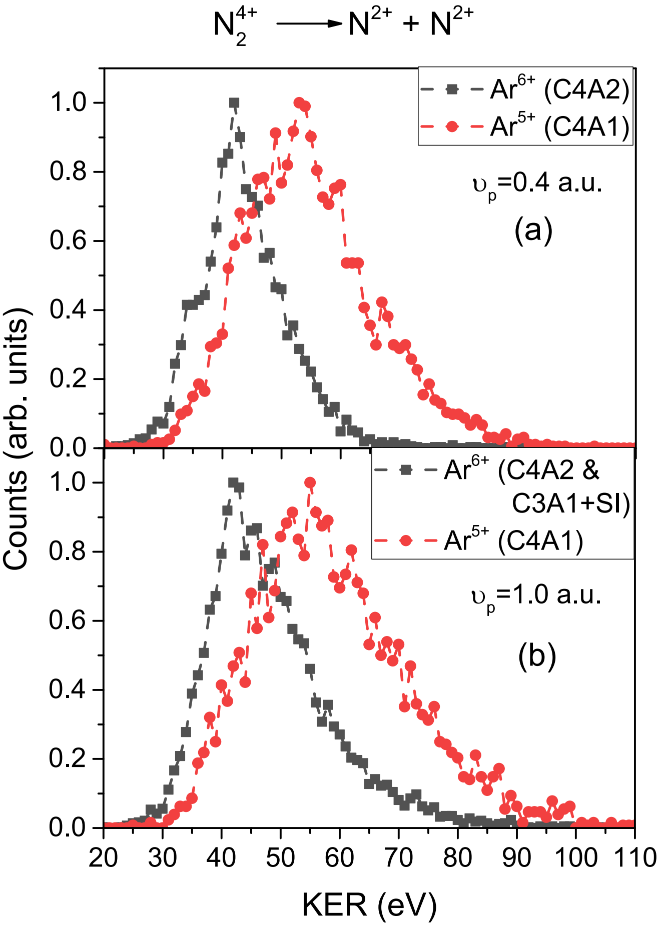

FIG. 7. Normalized KER spectra of the symmetric $\mathrm{N}^{2+} + \mathrm{N}^{2+}$ dissociation channel for different capture associated processes at (a) $\upsilon_p = 0.4$ a.u. and (b) 1.0 a.u.

The reaction windows for the (1111), (10111), and (01111) strings [cf. Fig. 4(c)] mostly stay in the double-autoionization region, which has a threshold of 166.13 eV [54] (DI energy of Ar^{4+}). The (4,4,4,5), (4,4,5,5), (4,4,4,4), and the higher l ($\geqslant 2$) of the (3,4,4,4) and (3,3,4,4) states stay in the double-autoionization region. For the (01111) string, the lower l (< 2) of the (3,4,4,4) and (3,3,4,4) stay in the single-autoionization regime. Double autoionization is the dominant process based on the reaction window and the available states. However, the single-autoionization process is accompanied by a radiative decay resulting in the second most dominant C4A1 process.

The KERDs of the $\mathrm{N}^{2+} + \mathrm{N}^{2+}$ dissociation channel for the C4A2 and C4A1 process peaked around 42.8 ± 0.4 and 53.0 ± 0.4 eV, respectively. The KERDs also spread to a wide range from 30 to 90 eV. In order to understand the origin of the broad KERDs, we recall the electron recapture process based on the ECOB model. Here, we have considered the (1111), (01111), and (10111) capture strings. In the case of (1111), four electrons are captured by the projectile and populate the ground and lower excited states of the N_2^{4+*} molecular ions with an FWHM ∼20.6 eV. The dissociation of these electronic states around the DL_{22} ($\mathrm{N}^{2+} + \mathrm{N}^{2+}$) dissociation limit results in lower and around-the-mean value (∼42.8 eV) of KERDs.

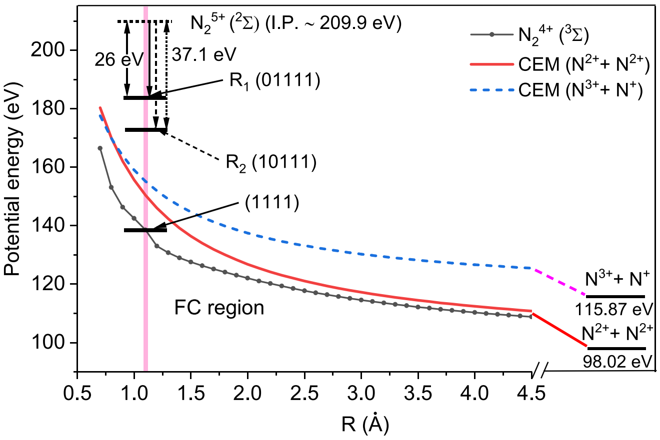

FIG. 8. Potential energy curve of the N_2^{4+} ($^3\Sigma$) ground electronic state (solid circles) is calculated by the CCSD method using the cc-pVDZ basis set. The potential energy is plotted with respect to the ground electronic state of the neutral N_2 ($^1\Sigma_g^+$) molecules. The solid and dashed lines represent the pure Coulomb explosion states for $N^{2+} + N^{2+}$ (DL_{22}) and $N^{3+} + N^+$ (DL_{31}), respectively. The dissociation energies are taken from these references [47,57]. Positions of the ground and probable excited electronic states for the (1111), (01111), and (10111) electron-capture strings are indicated by the solid horizontal lines around the FC region.

The (01111) string is a five-electron process where the target recaptures the first electron, and the projectile captures the other four electrons. Here, the first electron is recaptured to the excited states of N_2^{4+*} molecular ions situated around (209.9–26) = 183.9 eV with a FWHM ~6.7 eV. The ionization potential of the N_2^{5+} ($^2\Sigma$) ground electronic state is calculated to be around ~209.9 eV with respect to the ground electronic state of the neutral N_2 ($^1\Sigma_g^+$) molecules. We have named this recaptured process R_1. For the (10111) string, the target recaptures the second electron around (209.9–37.1) = 172.8 eV with a FWHM ~8.8 eV. This recapture path is named R_2. Dissociation of the highly excited states around the DL_{22} dissociation limit populated through the R_1 and R_2 paths results in the higher (KER $\geqslant$ 53 eV) KERDs. However, dissociating these electronic states to higher dissociation limits (> DL_{22}) would result in KERDs around the mean KER values. Figure 8 schematically shows the position of the lower and higher populated electronic states of the N_2^{4+} molecular ions. For the $N^{2+} + N^{2+}$ dissociation channel, the pure Coulomb dissociation state with KER around 52.8 eV is calculated using the following equation:

$$V(R) = 14.4\frac{2 \times 2}{R(\text{Å})} + DL_{22}, \tag{19}$$

where $V(R)$ represents the potential energy in eV.

For the intermediate collision velocity (υ_p = 1.0 a.u.), the capture path associated with the final Ar^{6+} projectile is the most dominant process with a relative yield of around 66.7 ± 0.7 %. The C4A2 process and C3A1 in addition to the SI (C3A1 + SI) process are the two possible capture paths. The relative yield of C4A2 increases with υ_p as the populations shifts towards the higher *nl* states. Also, the contribution of the C3A1 + SI process enhances the yield. In coincidence with the Ar^{5+} projectile, the C4A1 process could mix with C3A0 + SI. However, in the N_2^{3+} dissociation, we have seen that C3A0 has an almost negligible contribution. The mean KER values also shifted higher as the capture stabilization increased. The mean KER values are 45.4 ± 0.4 and 56.3 ± 0.4 eV for the corresponding C4A2/C3A1 + SI and C4A1 processes. The respective KER widths (FWHM) are 18.9 and 28.1 eV for the above capture paths.

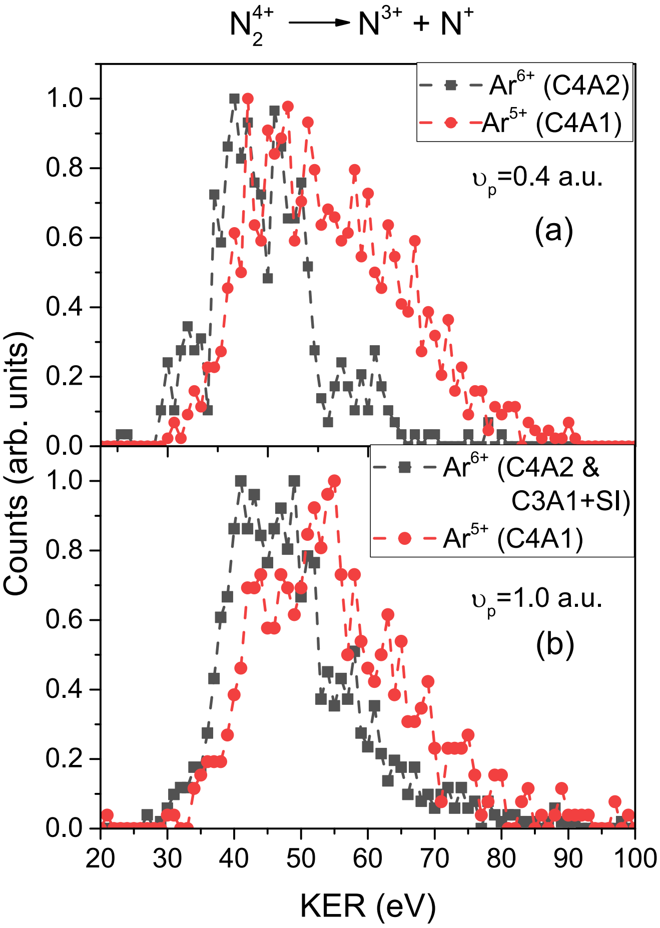

FIG. 9. Normalized KER spectra of the asymmetric $N^{3+} + N^+$ dissociation channel for different capture associated processes at (a) υ_p = 0.4 a.u. and (b) 1.0 a.u.

For the asymmetric channels, we have found that the KER values for different channels are centered around 33.2 ± 0.4, 43.4 ± 0.4, and 58.5 ± 0.4 eV (cf. Fig. 9). Contrary to the results in Ref. [32], we have not observed any low-energy KER peak below 30 eV. The origin of the presently measured different KER shoulderlike peaks can be explained by following different excited states' decays [31,32,53],

$$N_2^{4+}(a^5\Sigma) \rightarrow N^{3+}(^3P) + N^+(^3P), \quad \text{KER} = 33.10\text{eV} \tag{20}$$

and

$$N_2^{4+}(b^5\Sigma) \rightarrow N^{3+}(^3P) + N^+(^3P), \quad \text{KER} = 42.90\text{eV}. \tag{21}$$

For $\upsilon_p = 0.4$ a.u., the contributions from the two most dominant C4A1 and C4A2 channels are $66.1 \pm 2.1\%$ and $28.7 \pm 1.4\%$, respectively.

The C4A1 channel is more dominant for asymmetric channels, whereas C4A2 is relatively prevalent for symmetric channels. This can be explained as follows: in order to capture three electrons from the near-site N and one electron from the far-site N, the impact parameters have to be smaller. These collisions with smaller impact parameters results in the population of the lower projectile states. Due to the strong charge redistribution, such asymmetry is mostly equalized, but some may remain. Also, theKERDs similar to those of the symmetric channel indicate that the binding energies of the populated electronic states stay higher as the Coulomb dissociation limit stays higher for the asymmetric $N^{3+} + N^{+}$ dissociation than for the symmetric $N^{2+} + N^{2+}$ dissociation (cf. Fig. 8). The smaller impact parameters result in the populations of the high-lying electronic states of the molecular ions. Therefore, electrons are captured into the lower projectile states with less double-autoionization yield. From C4A2 to C4A1 processes, the KER window (FWHM) also broadened from 15.4 to 27.6 eV, and the mean KER peak shifted from 43.4 ± 0.4 to 52.2 ± 0.4 eV. Here also, the recapture of the loosely bound electrons leads to the higher KER values as discussed for the $N^{2+} + N^{2+}$ dissociation channel.

For $\upsilon_p = 1.0$ a.u., the capture process associated with the final Ar^{6+} projectile results in the most dominant process, with a contribution of $61.1 \pm 1.9\%$. This indicates populations shifted towards the higher *nl* states with higher double-autoionization yields. Also, the TI processes contribute to this collision velocity. The two possible capture paths are C4A2 and C3A1 in addition to SI, i.e., C3A1 + SI. The other dominant capture process is C4A1, which has contributions of around $35.3 \pm 1.5\%$. From the C4A2/C3A1 + SI to the C4A1 process, the mean KER value shifted from 46.0 ± 0.4 to 52.7 ± 0.4 eV and the corresponding KER window (FWHM) broadened from 17.2 to 23.5 eV.

The shoulderlike structures in the KERDs for different capture-associated channels imply the origin of the different non-Coulombic [31,53] excited states for both symmetric and asymmetric channels.

D. Dissociation of N_2^{5+}

The parent N_2^{5+} molecular ions dissociate into the quasisymmetric $N^{3+} + N^{2+}$ pair. The KERDs (cf. Fig. 10) show a shoulderlike peak around 65 eV and most probable KER values above 73 eV. The lower KER value (65.0 ± 0.4 eV) mostly results from the above $^2\Sigma$ electronic state. The existing KER value [32] for the decay channel is

$$N_2^{5+}(^2\Sigma) \rightarrow N^{3+}(^1S) + N^{2+}(^2P), \quad \text{KER} = 67.56\text{eV}. \quad (22)$$

The KER starting from 40 eV which is extended up to 135 eV indicates the dissociation of a large number of repulsive states. The reaction windows [cf. Fig. 4(d)] indicate that the possible combinations are (3,4,4,5,5), (3,4,4,4,4), (3,3,4,4,4), and (3,3,3,4,4). The Coulomb explosion energy (see Eq. (11)) for this channel is 78.7 eV.

For $\upsilon_p = 0.4$ a.u., the dominant projectile relaxation channels are quintuple-electron capture followed by double autoionization (C5A2) and quintuple-electron capture followed by single autoionization (C5A1). The relative contributions from the C5A2 and the C5A1 capture paths are $56.2 \pm 0.6\%$ and $39.1 \pm 0.5\%$, respectively. The mean KER value also shift from 71.7 ± 0.4 to 85.1 ± 0.4 eV as capture stabilization increases from C5A2 to C5A1. The corresponding KER width (FWHM) also broadens from 27.0 to 31.7 eV. For the less probable ($2.2 \pm 0.1\%$) C5A0 channel, the mean KER value peaks around 102.1 ± 0.4 eV, and the respective KER width (FWHM) is 39.4 eV.

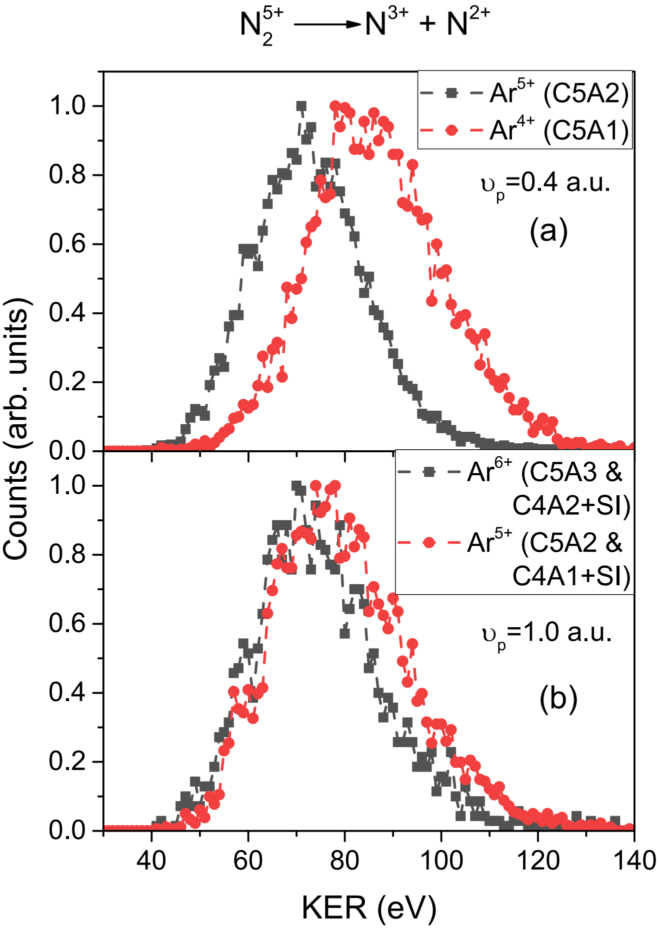

FIG. 10. Normalized KER spectra of the $N^{3+} + N^{2+}$ dissociation channel for different capture associated processes at (a) $\upsilon_p = 0.4$ a.u. and (b) 1.0 a.u.

For $\upsilon_p = 1.0$ a.u., the dominant capture paths are associated with the final projectile Ar^{5+} with a contribution of $67.6 \pm 0.9\%$. The possible capture processes are C5A2 and C4A1 in addition to SI (C4A1 + SI). We have neglected C3A0 in addition to the double ionization (DI) (C3A0 + DI) process, as both C3A0 and DI are less probable. For the final projectile Ar^{6+}, C5A3 and C4A2 in addition to SI (C4A2 + SI) is the second most probable channel with a contribution of $22.9 \pm 0.5\%$. Electrons are captured into the higher excited states ($n \geqslant 4$), which stay above the triple-autoionization threshold. From C5A3/C4A2 + SI to the C5A2/C4A1 + SI process, the corresponding mean KER value shifted from 72.9 ± 0.4 to 77.6 ± 0.4 eV. The corresponding KER width (FWHM) also broadens from 28.1 to 31.6 eV.

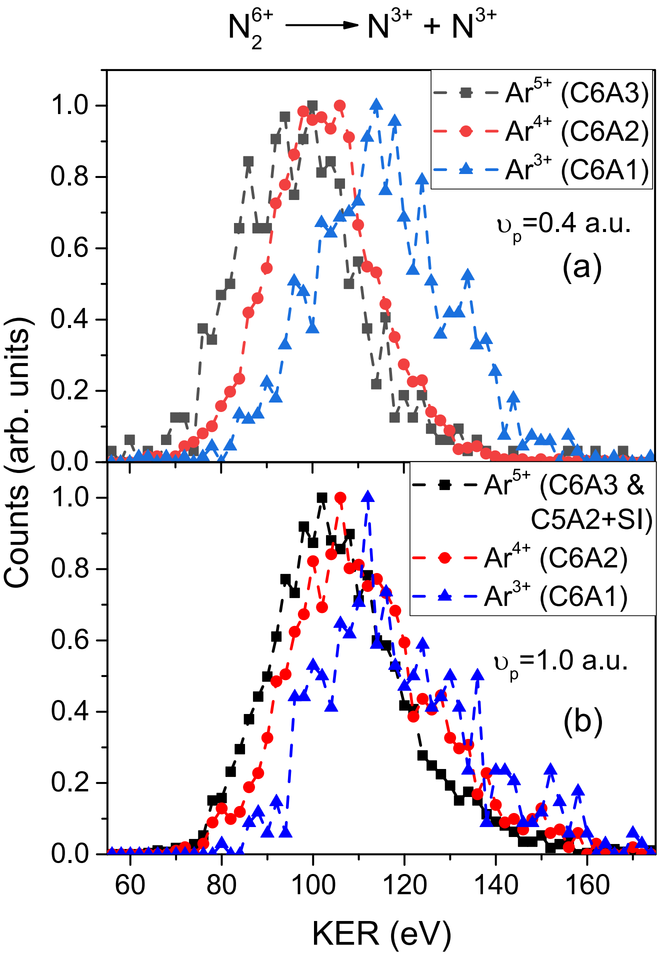

FIG. 11. Normalized KER spectra of the $N^{3+} + N^{3+}$ dissociation channel for different capture associated processes at (a) $\upsilon_p = 0.4$ a.u. and (b) 1.0 a.u.

E. Dissociation of N_2^{6+}

The parent N_2^{6+} molecular ion dissociates to the symmetric pair $N^{3+} + N^{3+}$ and the asymmetric $N^{4+} + N^{2+}$ channel. Here, we have limited our discussion to symmetric dissociation as the asymmetric channel is less probable, with insufficient data statistics. The KERDs (cf. Fig. 11) consist of the KER starting from 65 eV, and extending up to 170 eV. For sextuple-electron capture processes, the possible combinations are (3,3,4,4,5,5), (3,4,4,4,4,4), (3,3,4,4,4,4), and (3,3,3,4,4,4) [cf. Fig. 4(e)].

The available calculated KER values for these channels are as follows [31,32]:

$$N_2^{6+}(^1\Sigma) \rightarrow N^{3+}(^1S) + N^{3+}(^1S), \quad \text{KER} = 114.70\text{eV} \tag{23}$$

and

$$N_2^{6+}(^3\Pi) \rightarrow N^{3+}(^1S) + N^{3+}(^3P), \quad \text{KER} = 98.41\text{eV}. \tag{24}$$

For $\upsilon_p = 0.4$ a.u., the more probable capture paths are sextuple-electron capture followed by triple autoionization (C6A3), sextuple-electron capture followed by double autoionization (C6A2), and sextuple-electron capture followed by single autoionization (C6A1).

The C6A2 path has the highest yield, around $69.1 \pm 1.2\%$, and the corresponding KER mean is around 101.7 ± 0.4 eV. The other two contributing channels, C6A3 and C6A1, result in $9.8 \pm 0.4\%$ and $20.1 \pm 0.6\%$. Their respective mean KER values are 96.1 ± 0.4 and 114.4 ± 0.4 eV. For the C6A1 process, the KER width (FWHM) extends to a maximum of 39.4 eV.

For $\upsilon_p = 1.0$ a.u., dominant capture processes are associated with the final projectile Ar^{5+} with a contribution of $59.6 \pm 1.6\%$. The probable capture paths are C6A3 and C5A2 in addition to SI (C5A2 + SI). Enhancement of the C6A3 capture path is observed with increasing projectile velocity. It indicates that the enhancement of the projectile higher excited states populations relaxes through the triple-autoionization process. The mean KER value is around 103.9 ± 0.4 eV, and the corresponding KER width (FWHM) is 31.2 eV.

The CEM predicts [see Eq. (11)] the KER to be around 118 eV, which stays higher compared to our experimental results even for the C6A1 channel. The vacancy of the antibonding orbitals results in low KER values due to the enhancement of the chemical binding energy [31].

F. A comparative study: υ_p = 0.4 and 1.0 a.u.

At $\upsilon_p = 0.4$ a.u., ADC is the dominant capture process for the $N^+ + N^+$ dissociation channel. For the $N^{2+} + N^+$ dissociation channel, C3A1 is the dominant capture path. For N_2^{4+} dissociation, C4A1 and C4A2 contribute almost equally to the symmetric decay channel. On the other hand, the C4A1 process dominates the asymmetric decay channel. Therefore, single projectile autoionization dominates up to N_2^{4+} except for the symmetric $N^{2+} + N^{2+}$ decay channel where both are nearby. The double-autoionization (CmA2) yield increases for $m = 5$ and maximizes at $m = 6$. This C5A2 or C6A2 process implies that three electrons are easily populated into the excited states and ionized through the deexcitation of the N ($n = 4$) shell electrons. The relative yields for the above-discussed dissociation channels are given in Table I.

At $\upsilon_p = 1.0$ a.u., ADC is the most dominant process, and SC + SI also starts to contribute to the $N^+ + N^+$ dissociation channel. For $N^{2+} + N^+$ dissociation channel C3A1 is the dominant process. The contribution of C3A2 is enhanced and also ADC + SI contributes. For both symmetric and asymmetric decay of N_2^{4+}, the C4A2 process dominates, and the contributions of the C3A1 + SI process are enhanced. C5A2 and C4A1 + SI are the most dominant processes for the dissociating $N^{3+} + N^{2+}$ pair. $m = 4$ and 5 of the N_2^{4+} molecular ions result in the higher yield of the double-autoionization process. For the $N^{3+} + N^{3+}$ dissociation channel, C6A3 and C5A2 + SI result in the dominating process. For $m = 6$, triple autoionization is the dominant projectile relaxation process. The relative yields for all dissociation channels are given in Table II.

In coincidence with the same final projectile charge state, the mean KER values show a minor shift in higher values as υ_p increases from 0.4 to 1.0 a.u. (see Tables I and II). This was observed for the dissociating N_2^{m+} ($4 \leqslant m \leqslant 6$) molecular ions almost for every capture-associated process. The perturbation strengths (κ) for the 0.4 and 1.0 a.u. collision velocities are 20 and 8, respectively. One can think that the larger κ

induces a soft collision. However, the overall KERDs for the associated capture channels do not change significantly. It was seen that KERDs shifted to higher values as capture stabilization increased. With increasing $\upsilon_p = 0.4$ to 1.0 a.u., the yield of higher (double or triple) projectile autoionization increases. The enhancement of the population of higher *nl* states results in a larger autoionization yield [see Eq. (15)]. With increasing υ_p, the decrease of the fluorescence yield through the post-collision mechanisms (e.g., ATR mechanism) also enhances the relative yield of the autoionization process. These higher autoionization channels result in the dominant populations of the low-lying electronic states of the corresponding molecular ions. The overall KERDs, including all capture paths, are shifted to lower values as υ_p increases.

G. A classical capture model

As we have seen for N_2^{m+} decay channels, the mean KER spectrum shifts towards higher values as capture stabilization increases. The stabilization rates depend on the final projectile states involved in the processes. For TDC, we have already seen that the target electrons are captured in the closer shells of the projectile. The binding energy of the projectile stays higher for the (011) string than for the (11) string. The corresponding intermediate internuclear separation between the projectile ion and the target molecule is also smaller to access the shell by reducing the potential barrier. On the other hand, capturing the electrons in the higher states ($n, n' \geqslant n = 4$ or 5) could be easily accessible for large internuclear separations. The Coulomb potential energy curve [58,59] also shows that the system inelasticity (Q value) increases for capturing the electrons to lower projectile states. This also results in the smaller crossing radii (impact parameters) for the higher projectile binding energies as below:

$$V(R) = 14.4\,\frac{m \times (q-m)}{R(\text{Å})} - Q(\text{eV}) \tag{25}$$

and

$$R_m(\text{Å}) = 14.4\,\frac{m \times (q-m)}{Q(\text{eV})}. \tag{26}$$

Where m is the number of captured electrons. $V(R) = 0$ represents the classically allowed incoming capture channel, and R_m is the respective crossing radius.

In Fig. 12, we schematically present the above-discussed arguments based on the COB model. Tezuka *et al.* [60] also implemented a similar schematic model for the electron capture-induced dissociation of the triatomic molecules. These electrons in the higher states contribute to higher autoionization yield for multielectron captures.

Therefore, the higher stabilization, as in the C*m*A1 process (for $m > 3$), results in larger mean KER values than the other C*m*A2 or C*m*A3 channels. It is also observed that the separation of mean KER values between C*m*A1 and C*m*A2 channels is higher than the separation between C*m*A2 and C*m*A3 channels (cf. Figs. 10 and 11). It is well known that the energy differences ($\Delta E_n \propto \frac{1}{n_i^2} - \frac{1}{n_f^2}$) between the projectile states decrease with increasing n. This results in larger Q-value differences for the lower projectile states than the higher ones. The crossing radii for the higher projectile states do not differ much. Therefore, a small shift in mean KER values for the higher projectile autoionization channels is observed. For the higher capture stabilization channels, the width of the reaction window broadens as more bound electrons are captured. The broadening of KER width (FWHM) with the increment of the capture stabilization is consistent with the reaction window (cf. Fig. 4).

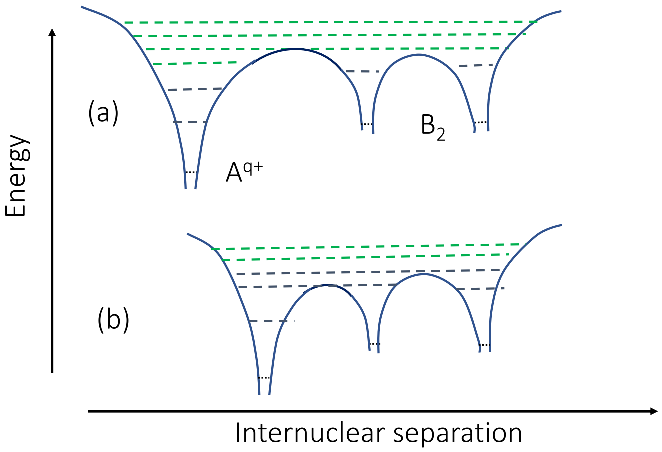

FIG. 12. Schematic representations of the electron capture mechanisms in the light of the COB model for highly charged ion-molecule collisions. (a) At large internuclear separations. (b) At relatively small internuclear separations.

VI. CONCLUSIONS

In conclusion, we present a detailed picture of the KERDs for dissociating N_2^{m+} ($2 \leqslant m \leqslant 6$) molecular ions in collision with Ar^{8+} projectiles. For this Ar^{8+}-N_2 collision system, our measurements cover the slow ($\upsilon_p = 0.4$ a.u.) and intermediate ($\upsilon_p = 1.0$ a.u.) collision velocities. The KERDs for each dissociation channel are measured in coincidence with the scattered projectiles, which separates the various projectile relaxation channels. For the multiple-electron capture processes, the reaction windows are also estimated using the ECOB model, which helps to identify the population of various projectile excited states.

Our study shows the projectile final states' dependence on the lower and higher KERDs of the $N^+ + N^+$ dissociation channel. For the TDC channel, reducing the higher KER region (C) indicates the reduction of the ATR mechanism with increasing υ_p. For the $N^{2+} + N^+$ dissociation channel, the KERDs shifted to higher values as capture stabilization increased. For the $N^{2+} + N^{2+}$, $N^{3+} + N^+$, $N^{3+} + N^{2+}$, and $N^{3+} + N^{3+}$ dissociation channels, the mean KER values shifted to higher values as capture stabilization increased. The higher KER values arise from recapturing the loosely bound electrons into the target highly excited states. The decay of these high-lying electronic states results in the higher KERDs, while more bound electrons are captured into the lower projectile states. For the N_2^{2+}, N_2^{3+} dissociation channels, C*m*A1 ($m \leqslant 3$) dominates for both υ_p. At $\upsilon_p = 0.4$ a.u., the C*m*A2 channel has the maximum yield for $4 \leqslant m \leqslant 6$ except for the asymmetric $N^{3+} + N^+$ dissociation where C4A1 dominates. At $\upsilon_p = 1.0$ a.u., C*m*A2 is the dominant capture path for both $m = 4$ and 5, while CmA3 is dominant for $m = 6$. The enhancement of the single or multiple projectile autoionizations indicates that the higher nl states populate with increasing υ_p. At $\upsilon_p = 1.0$ a.u., for the N_2^{m+} dissociation channels, the $(m - 1)$ electron capture, in addition to SI, is the contributing channel of the TI process. The reduction in the yield of capture stabilization with increasing υ_p results in a relatively lower mean KERDs. In these highly perturbative regimes, the KERDs for specific capture paths show a small variation with κ. A simple classical picture based on the COB model explains the impact parameter ranges of the lower and higher projectile states. Our results give an insight into the projectile state-dependent populations of the low- and high-lying electronic states of multiply charged molecular ions in highly perturbative HCI-molecule collisions.

ACKNOWLEDGMENTS

M.A.K.A.S. wishes to thank Dr. Priti from the National Institute of Fusion Science (NIFS), Japan for her help in understanding the FAC calculations. We want to thank the scientific staff for their help in the upkeep of the ECRIA Lab. This work is supported by the Department of Atomic Energy (Government of India) research project RTI 4002.

---

[1] R. Janev and H. Winter, State-selective electron capture in atom-highly charged ion collisions, Phys. Rep. **117**, 265 (1985).

[2] C.-D. Lin, *Review of Fundamental Processes and Applications of Atoms and Ions* (World Scientific, Singapore, 1993).

[3] A. A. Hasan, E. D. Emmons, G. Hinojosa, and R. Ali, Evidence for significant target outer-shell excitation in multiple-electron capture collisions of slow highly charged ions with many-electron atoms, Phys. Rev. Lett. **83**, 4522 (1999).

[4] H. Zhang, X. Fléchard, A. Cassimi, L. Adoui, G. Cremer, F. Frémont, and D. Hennecart, Experimental study of single, double, and multiple electron capture in slow $^{15}N^{7+}$ +Ne collisions using recoil-ion momentum spectroscopy, Phys. Rev. A **64**, 012715 (2001).

[5] E. D. Emmons, A. A. Hasan, and R. Ali, Multiple-electron capture processes in 70-keV $^{15}N^{7+}$-Ar collisions: A triple-coincidence study, Phys. Rev. A **60**, 4616 (1999).

[6] T. E. Cravens, X-ray emission from comets, Science **296**, 1042 (2002).

[7] P. Beiersdorfer, K. R. Boyce, G. V. Brown, H. Chen, S. M. Kahn, R. L. Kelley, M. May, R. E. Olson, F. S. Porter, C. K. Stahle, and W. A. Tillotson, Laboratory simulation of charge exchange-produced X-ray emission from comets, Science **300**, 1558 (2003).

[8] Z. Y. Song, X. C. Wang, Z. W. Li, K. L. Han, and D. Fischer, Evidence for target outer-shell excitation mediated by electron correlation in single-electron-capture collisions of slow He^{2+} ions with Ar atoms, Phys. Rev. A **102**, 042820 (2020).

[9] H. O. Folkerts, R. Hoekstra, and R. Morgenstern, Velocity and charge state dependences of molecular dissociation induced by slow multicharged ions, Phys. Rev. Lett. **77**, 3339 (1996).

[10] A. Niehaus, A classical model for multiple-electron capture in slow collisions of highly charged ions with atoms, J. Phys. B **19**, 2925 (1986).

[11] J. H. Posthumus and R. Morgenstern, Coincidences between electrons and target ions to identify capture channels in collisions of multiply charged ions on gas targets, Phys. Rev. Lett. **68**, 1315 (1992).

[12] I. Ali, R. D. DuBois, C. L. Cocke, S. Hagmann, C. R. Feeler, and R. E. Olson, Dynamics of the fragmentation of D_2 by fast protons and slow highly charged Xe^{23+}, Phys. Rev. A **64**, 022712 (2001).

[13] H. O. Folkerts, T. Schlathölter, R. Hoekstra, and R. Morgenstern, Dissociation of CO induced by ions: II. Dissociation pathways and states, J. Phys. B: At., Mol. Opt. Phys. **30**, 5849 (1997).

[14] R. Dörner, V. Mergel, O. Jagutzki, L. Spielberger, J. Ullrich, R. Moshammer, and H. Schmidt-Böcking, Cold target recoil ion momentum spectroscopy: A ‘momentum microscope’ to view atomic collision dynamics, Phys. Rep. **330**, 95 (2000).

[15] J. Ullrich, R. Moshammer, A. Dorn, R. Dörner, L. P. H. Schmidt, and H. Schmidt-Böcking, Recoil-ion and electron momentum spectroscopy: Reaction-microscopes, Rep. Prog. Phys. **66**, 1463 (2003).

[16] A. Khan, L. C. Tribedi, and D. Misra, A recoil ion momentum spectrometer for molecular and atomic fragmentation studies, Rev. Sci. Instrum. **86**, 043105 (2015).

[17] H. A. Bethe and R. Jackiw, *Intermediate Quantum Mechanics* (CRC, Boca Raton, 2018).

[18] E. Wells, T. Nishide, H. Tawara, R. L. Watson, K. D. Carnes, and I. Ben-Itzhak, Soft fragmentation of carbon monoxide by slow highly charged ions, Phys. Rev. A **77**, 064701 (2008).

[19] D. Mathur, Structure and dynamics of molecules in high charge states, Phys. Rep. **391**, 1 (2004).

[20] X. Ma, S. Zhang, W. Wen, Z. Huang, Z. Hu, D. Guo, J. Gao, B. Najjari, S. Xu, S. Yan, K. Yao, R. Zhang, Y. Gao, and X. Zhu, Atomic structure and collision dynamics with highly charged ions, Chin. Phys. B **31**, 093401 (2022).

[21] A. Khan, L. C. Tribedi, and D. Misra, Velocity and charge-state dependence on the Coulomb explosion of N_2, under the impact of highly-charged ions at intermediate velocities, J. Phys. B: At., Mol. Opt. Phys. **54**, 135201 (2021).

[22] R. Boll, J. M. Schäfer, B. Richard, K. Fehre, G. Kastirke, Z. Jurek, M. S. Schöffler, M. M. Abdullah, N. Anders, T. M. Baumann *et al.*, X-ray multiphoton-induced Coulomb explosion images complex single molecules, Nat. Phys. **18**, 423 (2022).

[23] J. Matsumoto, A. Leredde, X. Flechard, K. Hayakawa, H. Shiromaru, J. Rangama, C. L. Zhou, S. Guillous, D. Hennecart, T. Muranaka, A. Mery, B. Gervais, and A. Cassimi, Asymmetry in multiple-electron capture revealed by radiative charge transfer in Ar dimers, Phys. Rev. Lett. **105**, 263202 (2010).

[24] N. Neumann, D. Hant, L. P. H. Schmidt, J. Titze, T. Jahnke, A. Czasch, M. S. Schöffler, K. Kreidi, O. Jagutzki, H. Schmidt-Böcking, and R. Dörner, Fragmentation dynamics of CO_2^{3+} investigated by multiple electron capture in collisions with slow highly charged ions, Phys. Rev. Lett. **104**, 103201 (2010).

[25] X. Zhu, X. Hu, S. Yan, Y. Peng, W. Feng, D. Guo, Y. Gao, S. Zhang, A. Cassimi, J. Xu *et al.*, Heavy N^+ ion transfer in doubly

charged N_2Ar van der Waals cluster, Nat. Commun. **11**, 2987 (2020).

[26] A. Méry, A. N. Agnihotri, J. Douady, X. Fléchard, B. Gervais, S. Guillous, W. Iskandar, E. Jacquet, J. Matsumoto, J. Rangama, F. Ropars, C. P. Safvan, H. Shiromaru, D. Zanuttini, and A. Cassimi, Role of a neighbor ion in the fragmentation dynamics of covalent molecules, Phys. Rev. Lett. **118**, 233402 (2017).

[27] E. Gagnon, P. Ranitovic, X.-M. Tong, C. L. Cocke, M. M. Murnane, H. C. Kapteyn, and A. S. Sandhu, Soft X-ray-driven femtosecond molecular dynamics, Science **317**, 1374 (2007).

[28] B. Siegmann, U. Werner, R. Mann, N. M. Kabachnik, and H. O. Lutz, Kinetic energy release distributions in the Coulomb explosion of N_2 molecules induced by fast, highly-charged-ion impact, Phys. Rev. A **62**, 022718 (2000).

[29] H. Knudsen, H. K. Haugen, and P. Hvelplund, Single-electron-capture cross-section for medium- and high-velocity, highly charged ions colliding with atoms, Phys. Rev. A **23**, 597 (1981).

[30] T. Mizuno, T. Yamada, H. Tsuchida, Y. Nakai, and A. Itoh, Kinetic-energy release in N_2 fragmentation by charge-changing collisions of 2 MeV C^+ ions, Phys. Rev. A **82**, 054702 (2010).

[31] A. Remscheid, B. A. Huber, M. Pykavyj, V. Staemmler, and K. Wiesemann, Electron capture and dissociation of the molecule in slow collisions, J. Phys. B: At., Mol. Opt. Phys. **29**, 515 (1996).

[32] J. Rajput, S. De, A. Roy, and C. P. Safvan, Kinetic energy distributions and signature of target excitation in N_2 fragmentation on collisions with Ar^{9+} ions, Phys. Rev. A **74**, 032701 (2006).

[33] W. Groh, A. Muller, A. S. Schlachter, and E. Salzborn, Transfer ionisation in slow collisions of multiply-charged ions with atoms, J. Phys. B **16**, 1997 (1983).

[34] R. A. Phaneuf, F. W. Meyer, and R. H. McKnight, Single-electron capture by multiply charged ions of carbon, nitrogen, and oxygen in atomic and molecular hydrogen, Phys. Rev. A **17**, 534 (1978).

[35] A. N. Agnihotri, A. H. Kelkar, S. Kasthurirangan, K. V. Thulasiram, C. A. Desai, W. A. Fernandez, and L. C. Tribedi, An ECR ion source-based low-energy ion accelerator: development and performance, Phys. Scr. **2011**, 014038 (2011).

[36] M. A. K. A. Siddiki, M. Nrisimhamurty, K. Kumar, J. Mukherjee, L. C. Tribedi, A. Khan, and D. Misra, Development of a cold target recoil ion momentum spectrometer and a projectile charge state analyzer setup to study electron transfer processes in highly charged ion–atom/molecule collisions, Rev. Sci. Instrum. **93**, 113313 (2022).

[37] RoentDek Handels GmbH, https://www.roentdek.com.

[38] M. A. K. A. Siddiki, L. C. Tribedi, and D. Misra, Probing the fragmentation pathways of an argon dimer in slow ion-dimer collisions, Atoms **11**, 34 (2023).

[39] N. Bohr and J. Lindhard, On the properties of a gas of charged particles, K. Dan. Vidensk. Selsk. Mat.-Fys. Medd **28**, 7 (1954).

[40] J. X. Shao, X. M. Chen, Z. Y. Liu, R. Qi, and X. R. Zou, Multi-ionization of helium by slow highly charged ions, Phys. Rev. A **77**, 042711 (2008).

[41] J. X. Shao, X. M. Chen, X. R. Zou, X. A. Wang, and F. J. Lou, Simultaneous ionization of both collision partners in the strong perturbative energy range (20–500 keV/u), Phys. Rev. A **78**, 042701 (2008).

[42] M. Barat and P. Roncin, Multiple electron capture by highly charged ions at kev energies, J. Phys. B: At., Mol. Opt. Phys. **25**, 2205 (1992).

[43] H. Yuan, Z. Xu, S. Xu, C. Ma, Z. Zhang, D. Guo, X. Zhu, D. Zhao, S. Zhang, S. Yan, Y. Gao, R. Zhang, and X. Ma, Three-body fragmentation dynamics of CH_3CCH^{3+} investigated by 50-keV/u Ne^{8+} impact: Comparison with its isomer ion $CH_2CCH_2^{2+}$, Phys. Rev. A **105**, 022814 (2022).

[44] G. Herzberg, *Molecular Spectra and Molecular Structure* (D. van Nostrand, New York, 1945).

[45] M. A. Abdallah, W. Wolff, H. E. Wolf, E. Y. Kamber, M. Stöckli, and C. L. Cocke, Single and double electron capture from He by Ar^{16+} studied using cold-target recoil-ion momentum spectroscopy, Phys. Rev. A **58**, 2911 (1998).

[46] C. Wu, Y. Yang, Z. Wu, B. Chen, H. Dong, X. Liu, Y. Deng, H. Liu, Y. Liu, and Q. Gong, Coulomb explosion of nitrogen and oxygen molecules through non-Coulombic states, Phys. Chem. Chem. Phys. **13**, 18398 (2011).

[47] J. Dunning Jr., Gaussian basis sets for use in correlated molecular calculations. I. The atoms boron through neon and hydrogen, J. Chem. Phys. **90**, 1007 (1989).

[48] M. F. Gu, The flexible atomic code, Can. J. Phys. **86**, 675 (2008).

[49] B. Wang, J. Han, X. Zhu, L. Wei, B. Ren, Y. Zhang, W. Yu, S. Yan, X. Ma, Y. Zou, L. Chen, and B. Wei, Dissociative ionization of OCS induced by highly charged ion impact, Phys. Rev. A **103**, 042810 (2021).

[50] H. Bachau, P. Roncin, and C. Harel, Stabilization of autoionizing states during ion-atom collisions, J. Phys. B: At., Mol. Opt. Phys. **25**, L109 (1992).

[51] S. Martin, J. Bernard, A. Denis, J. Désesquelles, L. Chen, and Y. Ouerdane, Velocity dependence of stabilized double electron capture in N^{7+} + Ar collisions, Nucl. Instrum. Methods Phys. Res., Sect. B **98**, 270 (1995), special issue: The Physics of Highly Charged Ions.

[52] S. Martin, J. Bernard, L. Chen, A. Denis, and J. Désesquelles, Stabilized double-electron capture in Ne^{10+}-He collisions: Velocity dependence of Rydberg-electron n, l distributions, Phys. Rev. A **52**, 1218 (1995).

[53] C. P. Safvan and D. Mathur, Dissociation of highly charged N_2^{q+} ($q \geqslant 2$) ions via non-Coulombic potential energy curves, J. Phys. B: At., Mol. Opt. Phys. **27**, 4073 (1994).

[54] NIST: Atomic Spectra Database, Energy Levels, https://physics.nist.gov/PhysRefData/ASD/levels_form.html.

[55] E. Wells, V. Krishnamurthi, K. D. Carnes, N. G. Johnson, H. D. Baxter, D. Moore, K. M. Bloom, B. M. Barnes, H. Tawara, and I. Ben-Itzhak, Proton-carbon monoxide collisions from 10 keV to 14 MeV, Phys. Rev. A **72**, 022726 (2005).

[56] B. Ding, D. Yu, C. Shao, R. Lu, F. Ruan, H. Li, W. Zhang, and X. Cai, Multielectron processes in collisions of Xe^{23+} ions with Ar atoms, Eur. Phys. J. D **65**, 391 (2011).

[57] G. Herzberg and L. Herzberg, Rotation-vibration spectra of diatomic and simple polyatomic molecules with long absorbing paths XI. The spectrum of carbon dioxide (CO_2) below 1.25μ, J. Opt. Soc. Am. **43**, 1037 (1953).

[58] P. Roncin, M. Barat, and H. Laurent, Differential cross-sections for one- and two-electron capture by highly charged ions (N^{7+}, O^{7+}, O^{8+}, Ne^{7+}, Ne^{8+}) at low keV energies, Europhys. Lett. **2**, 371 (1986).

[59] H. Laurent, M. Barat, M. N. Gaboriaud, L. Guillemot, and P. Roncin, Differential cross sections and electron transfer mechanisms in multiply charged ion-atom collisions, J. Phys. B **20**, 6581 (1987).

[60] H. Tezuka, K. Takahashi, J. Matsumoto, R. Karimi, J. H. Sanderson, and H. Shiromaru, Correlated formation of the excited states of recoil and scattered ions in multiple electron capture collision of Ar^{8+} with CO_2 and OCS, J. Phys. B: At., Mol. Opt. Phys. **51**, 035202 (2018).